nature

LETTERS

despite the possibility of scattering to the lower indirect valleys.

With a reverse bias from 0 to 4 V, both peaks are red shifted by the QCSE. The e–hh exciton is shifted from 1,408 nm (0 V) to 1,456 nm (4 V). The maximum effective electro-absorption coefficient change is 2,800 cm^{-1} at 1,438 nm under 3 V bias. This is, to our knowledge, the first efficient electro-absorption modulation observed in group-IV materials, and its performance is comparable to high-quality (direct gap) III–V materials at similar wavelengths (see, for example, ref. 19). The clarity of the exciton peaks in the presence of a field is actually better than that of typical III–V structures at such wavelengths[24], and the electroabsorption shows much clearer shifts than previous electroabsorption measurements in indirect III–V materials[25]. With a 4 V bias, the absorption coefficient contrast is greater than 3 over a bandwidth ranging from 1,443 to 1,471 nm, with a peak value of 4.69 at 1,461 nm.

The possibility of operating different quantum-well designs at, say, 1,550 nm, which is compatible with long-distance telecommunications, will be the subject of future work. We also anticipate that waveguide modulator structures will be realizable using appropriate materials for waveguide cladding layers.

The measured shift agrees with simulated results (Fig. 4) obtained via the tunnelling resonance method[5,18]. In addition, we evaluated the exciton binding energy shift as in ref. 18, using numerically evaluated electron and hole wavefunctions, though this correction is <1 meV and is neglected here. We used a Γ-valley electron effective mass of $0.041m_o + 0.115(1 − x)m_o$, and a heavy-hole effective mass of $0.28m_o + 0.21(1 − x)m_o$, where m_o is the free electron mass and x is the Ge concentration[26,27] (the relevant silicon (001) hole mass is based on Luttinger parameters[28]).

We have demonstrated efficient QCSE in silicon-based structures, using strained Ge MQWs. The behaviour of the exciton peaks, the band edge shift and the shift in absorption coefficient are comparable to those observed in III–V materials at similar wavelengths. Our materials and fabrication processes are completely CMOS compatible and suitable for mass production. This approach is therefore very promising for silicon-based electro-absorption modulators operating at high speed, low power, low operating voltage and with small device areas.

1. Miller, D. A. B. Rationale and challenges for optical interconnects to electronic chips. *Proc. IEEE* 88, 728–749 (2000).
2. Liu, A. et al. A high-speed silicon optical modulator based on a metal-oxide-semiconductor capacitor. *Nature* 427, 615–618 (2004).
3. Xu, Q., Schmidt, B., Pradhan, S. & Lipson, M. Micrometre-scale silicon electro-optic modulator. *Nature* 435, 325–327 (2005).
4. Soref, R. A. & Bennett, B. R. Electrooptical effects in silicon. *IEEE J. Quant. Electron.* 23, 123–129 (1987).
5. Miller, D. A. B. et al. Band-edge electroabsorption in quantum well structures: the quantum-confined Stark effect. *Phys. Rev. Lett.* 53, 2173–2176 (1984).
6. Arad, U. et al. Development of a large high-performance 2-D array of GaAs-AlGaAs multiple quantum-well modulators. *IEEE Photon. Tech. Lett.* 15, 1531–1533 (2003).
7. Liu, C. P. et al. Design, fabrication and characterisation of normal-incidence 1.56-μm multiple-quantum-well asymmetric Fabry-Perot modulators for passive picocells. *IEICE Trans. Electron. E* 86C, 1281–1289 (2003).
8. Cressler, J. D. SiGe HBT technology: a new contender for Si-Based RF and microwave-circuit applications. *IEEE Trans. Microwave Theory Tech.* 46, 572–589 (1998).
9. Qasaimeh, O., Bhattacharya, P. & Croke, E. T. SiGe-Si quantum-well electroabsorption modulators. *IEEE Photon. Tech. Lett.* 10, 807–809 (1998).
10. Miyake, Y., Kim, J. Y., Shiraki, Y. & Fukatsu, S. Absence of Stark shift in strained Si₁₋ₓGeₓ/Si type-I quantum wells. *Appl. Phys. Lett.* 68, 2097–2099 (1996).
11. Li, C. et al. Observation of quantum-confined Stark shifts in SiGe/Si type-I multiple quantum wells. *J. Appl. Phys.* 87, 8195–8197 (2000).
12. Park, J. S., Karunasiri, R. P. G. & Wang, K. L. Observation of large Stark shift in Ge₁₋ₓSiₓ/Si multiple quantum wells. *J. Vac. Sci. Technol. B* 8, 217–220 (1990).
13. Yakimov, A. I. et al. Stark effect in type-II Ge/Si quantum dots. *Phys. Rev. B* 67, 125318 (2003).
14. Lewen, R., Irmscher, S., Westergren, U., Thylen, L. & Eriksson, U. Segmented transmission-line electroabsorption modulators. *J. Lightwave Technol.* 22, 172–179 (2004).
15. Krishnamoorthy, A. V. & Miller, D. A. B. Scaling optoelectronic-VLSI circuits into the 21ˢᵗ century: a technology roadmap. *IEEE J. Select. Top. Quant. Electron.* 2, 55–76 (1996).
16. Kibar, O., Van Blerkom, D. A., Fan, C. & Esener, S. C. Power minimization and technology comparisons for digital free-space optoelectronic interconnections. *J. Lightwave Technol.* 17, 546–555 (1999).
17. Cho, H., Kapur, P. & Saraswat, K. C. Power comparison between high-speed electrical and optical interconnects for interchip communication. *J. Lightwave Technol.* 22, 2021–2033 (2004).
18. Miller, D. A. B. et al. Electric field dependence of optical absorption near the bandgap of quantum well structures. *Phys. Rev. B* 32, 1043–1060 (1985).
19. Helman, N. C., Roth, J. E., Bour, D. P., Altug, H. & Miller, D. A. B. Misalignment-tolerant surface-normal low-voltage modulator for optical interconnects. *IEEE J. Select. Top. Quant. Electron.* 11, 338–342 (2005).
20. Schmitt-Rink, S., Chemla, D. S., Knox, W. H. & Miller, D. A. B. How fast is excitonic electroabsorption? *Opt. Lett.* 15, 60–62 (1990).
21. Maslov, A. V. & Citrin, D. S. Quantum-well optical modulator at terahertz frequencies. *J. Appl. Phys.* 93, 10131–10133 (2003).
22. Galdin, S., Dollfus, P., Aubry-Fortuna, V., Hesto, P. & Osten, H. J. Band offset predictions for strained group IV alloys: Si₁₋ₓ₋ᵧGeₓCᵧ on Si(001) and Si₁₋ₓGeₓ on Si₁₋ᵧGeᵧ(001). *Semicond. Sci. Technol.* 15, 565–572 (2000).
23. Rieger, M. M. & Vogl, P. Electronic-band parameters in strained Si₁₋ₓGeₓ alloys on Si₁₋ᵧGeᵧ substrates. *Phys. Rev. B* 48, 14276–14287 (1993).
24. Schaffler, F. High-mobility Si and Ge structures. *Semicond. Sci. Technol.* 12, 1515–1549 (1997).
25. Goossen, K. W., Yan, R. H., Cunningham, J. E. & Jan, W. Y. AlₓGa₁₋ₓAs-AlAs quantum well surface-normal electroabsorption modulators operating at visible wavelengths. *Appl. Phys. Lett.* 59, 1829–1831 (1991).
26. Crow, G. C. & Abram, R. A. Monte Carlo simulations of hole transport in SiGe and Ge quantum wells. *Semicond. Sci. Technol.* 15, 7–14 (2000).
27. Dresselhaus, G., Kip, A. F. & Kittel, C. Cyclotron resonance of electrons and holes in silicon and germanium crystals. *Phys. Rev.* 98, 368–384 (1955).
28. Lawaetz, P. Valence-band parameters in cubic semiconductors. *Phys. Rev. B* 4, 3460–3467 (1971).

Figure 4 | Shifts of exciton peaks. Comparison of heavy-hole exciton peak shift from measurements (filled squares) and tunnelling resonance calculations (sum of electron and hole level shifts) (line).

Unidirectional molecular motor on a gold surface

Richard A. van Delden[1], Matthijs K. J. ter Wiel[1], Michael M. Pollard[1], Javier Vicario[1], Nagatoshi Koumura[1] & Ben L. Feringa[1]

Molecules capable of mimicking the function of a wide range of mechanical devices have been fabricated, with motors that can induce mechanical movement attracting particular attention[1,2]. Such molecular motors convert light or chemical energy into directional rotary or linear motion[3–10], and are usually prepared and operated in solution. But if they are to be used as nano-machines that can do useful work, it seems essential to construct systems that can function on a surface, like a recently reported linear artificial muscle[11]. Surface-mounted rotors have been realized and limited directionality in their motion predicted[12,13]. Here we demonstrate that a light-driven molecular motor capable of repetitive unidirectional rotation[14] can be mounted on the surface of gold nanoparticles. The motor design[14] uses a chiral helical alkene with an upper half that serves as a propeller and is connected through a carbon–carbon double bond (the rotation axis) to a lower half that serves as a stator. The stator carries two thiol-functionalized 'legs', which then bind the entire motor molecule to a gold surface. NMR spectroscopy reveals that two photo-induced *cis-trans* isomerizations of the central double bond, each followed by a thermal helix inversion to prevent reverse rotation, induce a full and unidirectional 360° rotation of the propeller with respect to the surface-mounted lower half of the system.

Inspired by the ATP-ase system[15], we constructed an artificial surface-mounted motor schematically shown in Fig. 1a. The design of the motor molecule 1 is based on a second-generation[14] light-driven rotary motor 2 with a symmetric lower half bearing two methoxy substituents (Fig. 1b). Replacing these groups by two C₆-spacers terminated with thiols (as shown in structure 1) allowed self-assembly onto a gold surface, providing 1-Au. Gold nanoparticles are particularly appropriate for our purpose, as chromophore functionalized nanoparticles are well studied[16] and photochromism of azobenzenes[17] and electrochemical switching of rotaxanes[18] attached to such nanoparticles has been demonstrated. Two points of attachment are essential to prevent uncontrolled thermal rotation of the entire system with respect to the surface. The C₆-spacer should diminish direct (electronic) interaction between the chromophores and the Au surface (which might influence the excited state processes) and give the separate photo-active moieties sufficient free volume to perform the anticipated rotary motion. On the basis of the dynamic processes in structurally related molecular motors[14], 1-Au was expected to exhibit photochemical and thermal isomerization processes, as shown in Fig. 1c.

Two energetically uphill photochemical isomerization steps (steps 1 and 3 in Fig. 1) each followed by an energetically downhill irreversible thermal helix inversion step (steps 2 and 4 in Fig. 1) result in a full 360° rotation of one half of the molecule with respect to the other. The direction of rotation is controlled by the configuration at the stereogenic centre. Crucial is a strong energetic preference for the methyl substituent to adopt a pseudo-axial orientation. Irradiation
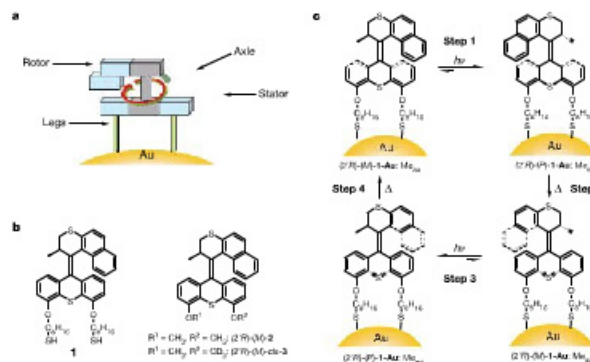

Figure 1 | Molecular motor anchored to a surface. a, Design of a surface-bound rotary motor. The system consists of a rotor connected via an axle (axis of rotation) to a stator part that is bound to a gold surface via two legs. **b,** Structure of motor 1 for surface studies and 2, 3 for solution studies; 1-Au denotes motor molecule 1 assembled onto Au. *R* denotes absolute configuration at the stereogenic centre; *M* and *P* denote helicity of the molecule. **c,** The four-state unidirectional rotation of functionalized nanoparticle 1-Au is shown (*hν*, photochemical step; Δ, thermal step). The photoisomerizations were induced by irradiation at λ = 280 nm or λ = 365 nm. Me_ax indicates the pseudo-axial orientation of the methyl substituent, Me_eq indicates the unstable pseudo-equatorial orientation of the methyl substituent.

[1]Department of Organic Chemistry, Stratingh Institute, University of Groningen, Nijenborgh 4, 9747 AG Groningen, The Netherlands.

of the stable $(2'R)$-(M)-isomer of **1-Au** with a pseudo-axial methyl substituent effects a *cis → trans* isomerization, which inverts the helicity of the system to form the $(2'R)$-(P)-isomer. Consequently, the methyl substituent is forced to adopt an energetically disfavoured pseudo-equatorial orientation. Upon heating, this unstable isomer undergoes a helix inversion resulting in the formation of the initial $(2'R)$-(M)-isomer, after a net 180° rotation of the upper half of the molecule in an anticlockwise fashion with respect to the lower half. This sequence is repeated in steps 3 and 4 to complete a full rotary cycle. The unidirectionality of the rotary process is ensured by the irreversibility of the thermal helix inversion steps.

Target compound **2** (4,5-dimethoxy-9-(2',3'-dihydro-2'-methyl-1'H-naphtha[2,1-b]thiopyran-1'-ylidene)-9H-thioxanthene; Fig. 1b), which serves as a precursor and a solution phase model for **1-Au**, was synthesized by adapted methods used for second-generation motors[10]. The $(2'R)$-(M)-**2** stereoisomer was resolved by chiral high-performance liquid chromatography (HPLC) and the absolute stereochemistry unequivocally assigned based on circular dichroism (CD) spectroscopy and X-ray analysis (see Supplementary Table 1). Starting from $(2'R)$-(M)-**2**, deprotection of the methoxy-substituents and introduction of two octylthiol moieties was achieved by standard synthetic techniques. Nanoparticles $(2'R)$-(M)-**1-Au** were prepared by the Brust-Schiffrin method[19] and characterized by dynamic light scattering (DLS), transmission electron microscopy (TEM) (Supplementary Fig. 11), and spectroscopic methods (for ultraviolet/visible (UV/Vis) and CD spectroscopy see Fig. 2, and for additional CD, UV, NMR, Fourier transform infrared (FT-IR) and surface enhanced Raman spectroscopy, see Supplementary Figs 2, 3, 4, 7–9 and 10, respectively).

The UV/Vis and CD spectra of $(2'R)$-(M)-**1-Au** and $(2'R)$-(M)-**2**

are characteristic of helical overcrowded alkenes (Fig. 2). The CD spectra of **1-Au** and **2** (Fig. 2a) are nearly identical because they solely reflect the helical chirality of the diaryl alkene moieties and confirm the (M)-helicity of **1-Au** and **2**. The UV/Vis spectrum of **1-Au** (Fig. 2b) is a superposition of the spectral bands of the motor moieties and a broad absorption of the nanoparticle, reaching far into the visible region (see Supplementary Fig. 2).

TEM data, together with the molar quantity of olefin moieties per gram of nanoparticles (as determined by CD spectroscopy) and the known density of gold (19.3 g cm^{-3})[20], gives the average overall formula of one nanoparticle of **1-Au** Au$_{251}$((S(CH$_2$)$_8$O)$_2$-C$_{27}$H$_{18}$S$_2$)$_{19}$. It can be calculated that for **1** there is only ~0.23 nm^2 surface area per linked sulphur atom; this can be compared with the surface area of alkanethiols on a flat Au surface as determined by electron diffraction studies (0.214 nm^2)[21].

The combined photochemical and thermal processes were investigated spectroscopically in toluene solution. The presented data for **1-Au** are in full agreement with those of the parent (model and control) compound **2**, unless indicated.

A 1.035×10^{-5} M solution (chromophore concentration) of $(2'R)$-(M)-**1-Au** in toluene at room temperature was irradiated (wavelength $\lambda \geq 280$ nm) until a photostationary state (PSS) was reached. The approximate inversion of the CD spectrum upon irradiation (Fig. 2a) indicates the change in helicity going from $(2'R)$-(M)-**1-Au** to $(2'R)$-(P)-**1-Au** (step 1 in Fig. 1c). In the UV/Vis spectrum a decrease in the intensity of the high wavelength band is indicative of the formation of $(2'R)$-(P)-**1-Au** (Fig. 2b). Clear isosbestic point(s) in both CD and UV/Vis spectra for the photo-chemical and thermal steps support clean isomerization processes (Fig. 2). From the UV/Vis spectra of $(2'R)$-(M)-**2** and $(2'R)$-(P)-**2**, the ideal wavelength for the formation of the unstable isomer was determined to be 365 nm. Subsequent irradiation of $(2'R)$-(M)-**1-Au** at this wavelength indeed resulted in a more selective isomerization with an associated increase in intensity of the CD bands (Fig. 2a) and an anticipated PSS of approximately 94:6. UV/Vis and CD data are consistent with this observation (Fig. 2).
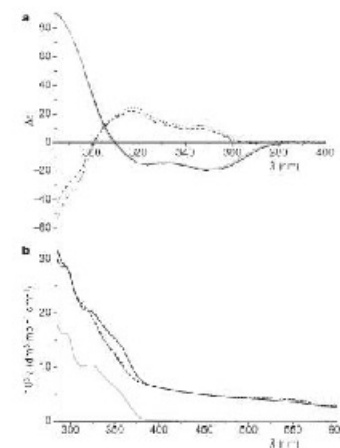
Subsequent heating of the PSS sample of $(2'R)$-(P)-**1-Au** $(T \geq 50\,°C)$ resulted in full conversion of unstable $(2'R)$-(P)-**1-Au** to stable $(2'R)$-(M)-**1-Au**, as a result of the thermal helix inversion (step 2 in Fig. 1c). It was verified that rotary motion occurs while motor **1-Au** remains bound to the surface; this was indicated by the presence of exclusively broad signals in the ^{1}H NMR spectrum (no trace of free motor in solution could be detected) after either heating the sample at 70°C for 2h or irradiation for 3h at 365 nm. Subsequent KCN mediated etching of the gold core of this sample of **1-Au** after 3h irradiation at 365 nm revealed unbound unstable and stable motor in a 2.5:1 ratio.

The kinetics of this helix inversion were determined by monitoring

the change in CD intensity with time at various temperatures $(T = 323, 333, 343, 353\,K)$, providing the rate constant (k_1) which was used to calculate the Gibbs free energy of activation $(\Delta^{\ddagger}G° = 96 \pm 2\,kJ\,mol^{-1})$ for the $(2'R)$-(P)-**1-Au** to $(2'R)$-(M)-**1-Au** interconversion using the Eyring equation. The slightly higher barrier than found for **2** in solution $(\Delta^{\ddagger}G° = 94 \pm 2\,kJ\,mol^{-1})$ can be attributed to the reduction in the degrees of freedom of the molecule when grafted onto the Au surface. At room temperature (293 K), the half-life for thermal helix inversion has almost doubled going from **2** $(t_{\frac{1}{2}} = 56 \times 10^2\,s)$ to **1-Au** $(t_{\frac{1}{2}} = 12 \times 10^3\,s)$. After the light-induced energetically uphill process $(2'R)$-(M)-**1-Au** to $(2'R)$-(P)-**1-Au** (step 1 in Fig. 1c) followed by a thermal energetically

Figure 2 | CD and UV spectra of 1-Au and 2. CD (**a**) and UV/Vis (**b**) spectra of pure $(2'R)$-(M)-1-Au (solid black lines), PSS$_{\geq 280nm}$ (dashed black) and PSS$_{365nm}$ (dotted black) samples (all spectra are adjusted for molar concentration of chromophores), and CD (**a**) and UV/Vis (**b**) spectrum of $(2'R)$-(M)-2 (solid grey) in toluene. After heating of the PSS samples $(T > 50\,°C)$, the original spectra of $(2'R)$-(M)-1-Au and $(2'R)$-(M)-2 were obtained.
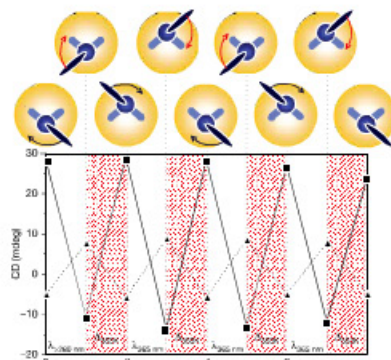

Figure 3 | Following two full turns by CD spectroscopy. Schematic representation of the unidirectional rotation of **1** (as viewed along the rotation axis) and two full four-stage 360° rotary cycles followed by CD spectroscopy. The change in CD intensity (mdeg) at 290 nm (solid line) and 320 nm (dashed) at each photochemical ($h\nu_{\lambda \geq 280nm}$ and $h\nu_{\lambda = 365nm}$) and thermal ($\Delta_{\geq 50K}$) isomerization step is shown.

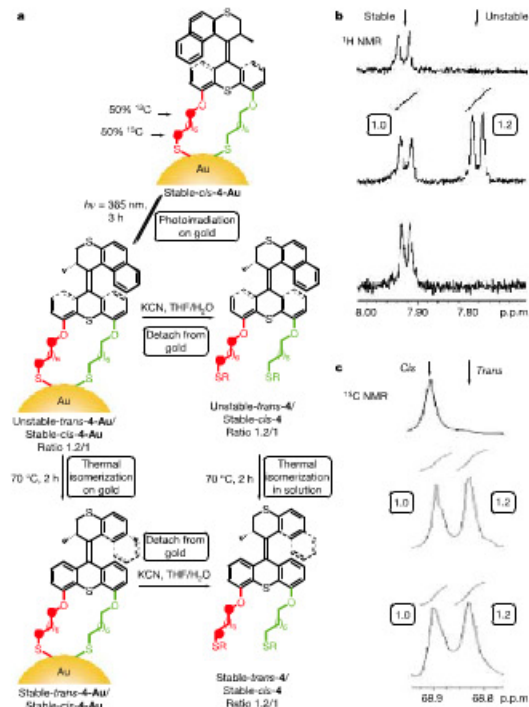**Figure 4 | Confirmation of unidirectional rotation on the nanoparticle using NMR spectroscopy.** **a**, Photochemical and thermal isomerization of ^{13}C isotope labelled motor **4** on gold (4-Au) and structures of major isomers of 4-Au. Cleaved motor probably exists as a mixture of free thiol (R = H) and disulphide (R = S-Motor). **b**, Key signals (ArH) in the ^{1}H NMR of stable-*cis*-4 in solution (top panel), after irradiation of stable-*cis*-4-Au and core etching (middle panel) and after irradiation of stable-*cis*-4-Au, heating, then etching (bottom panel). **c**, Key signals (-O^{13}CH$_2$[CH$_2$]$_7$) in the ^{13}C

NMR of stable-*cis*-4 in solution (top panel), after irradiation of stable-*cis*-4-Au and core etching, and subsequent heating (middle panel), and after irradiation of stable-*cis*-4-Au, heating, then etching (bottom panel). The conversion of stable isomer 4-Au to unstable isomer 4-Au (evaluated by ^{1}H NMR) matched the final conversion of stable-*cis*-4-Au to stable-*trans*-4-Au evaluated by ^{13}C NMR. In both cases, NMR analysis was performed after detachment.

downhill helix inversion (2′R)-(P)-1-**Au** to (2′R)-(M)-1-**Au** (step 2 in Fig. 1c), the upper rotor half of the molecule has performed a half rotation in an anticlockwise direction with respect to the lower half. Performing the same two-step process repeatedly results in continual unidirectional rotary motion. The state of the motor can be followed by CD spectroscopy, as is shown (Fig. 3) for two consecutive 360° cycles.

To confirm that the introduction of the two legs in the lower part of the molecule does not affect the four-stage unidirectional rotary process, we studied (2′R)-(M)-3, which has a non-symmetrical lower part with one OCH₃ and one OCD₃ (see Fig. 1b). These groups have negligible influence on the photochemical and thermal behaviour, and allowed the detection by NMR of all four steps in the rotary cycle (see Supplementary Information, Section 3).

Unequivocal proof for the unidirectionality of the motor attached to gold nanoparticles was achieved with isotope labelled motor 4-**Au** (Fig. 4). The only difference between 1-**Au** and 4-**Au** is that one leg in the latter compound contains a ¹³C isotope at the two positions flanking the stator and the surface bound thiol. The two distinct legs created in this way allow accurate detection by ¹H and ¹³C NMR of the isomers after photochemical and thermal steps on the surface, as illustrated in Fig. 4a.

The stable cis-isomer of 4 bound to the gold (cis-4-**Au**) was irradiated at 365 nm wavelength, and the sample split into two portions. The first portion was treated (KCN/THF/H₂O) so as to detach the motor from the surface to provide a mixture of the trans-unstable-4 and cis-stable-4 (ratio 1.2:1, ¹H NMR analysis, Fig. 4b). Subsequent thermal isomerization in toluene solution resulted in stable trans-4 and stable-cis-4 (ratio 1.2:1 ratio, ¹³C NMR analysis Fig. 4c).

The second portion was heated (70 °C, 2 h) to induce thermal isomerization of the motor while still on the gold surface (unstable-trans-4-**Au** to stable-trans-4-**Au**). Subsequent cleavage (KCN/THF/H₂O) of the motor from the gold provided an identical mixture of stable-trans-4 and stable-cis-4. These data show that the photochemical conversion of the stable form of 4-**Au** to the unstable form of 4-**Au** (¹H NMR analysis) correlates perfectly with the formation of stable trans-4-**Au** from stable cis-4-**Au** (¹³C NMR analysis).

The combined results (from CD studies of optically active (2′R)-(M)-1-**Au**, and NMR studies of ¹³C isotopically labelled 4-**Au**, with distinct legs) provide compelling evidence for the unidirectionality of the rotary process on the surface. We expect that the successful formation of fully functional surface-mounted rotors will enable investigation of the concerted action of a large ensemble of unidirectional molecular motors, and that this system might be a first step towards the construction of more elaborate and functional nanosized mechanical devices.

1. Balzani, V., Venturi, M. & Credi, A. Molecular Devices and Machines—A Journey into the Nanoworld (Wiley-VCH, Weinheim, 2003).
2. van Delden, R. A., ter Wiel, M. K. J., Koumura, N. & Feringa, B. L. in Molecular Motors (ed. Schliwa, M.) Ch. 23, 559–577 (Wiley-VCH, Weinheim, 2003).
3. Koumura, N., Zijlstra, R. W. J., van Delden, R. A., Harada, N. & Feringa, B. L. Light-driven monodirectional molecular rotor. Nature 401, 152–155 (1999).
4. Kelly, T. R., De Silva, H. & Silva, R. A. Unidirectional rotary motion in a molecular system. Nature 401, 150–152 (1999).
5. Leigh, D. A., Wong, J. K. Y., Dehez, F. & Zerbetto, F. Unidirectional rotation in a mechanically interlocked molecular rotor. Nature 424, 174–179 (2003).
6. Anelli, P. L., Spencer, N. & Stoddart, J. F. A molecular shuttle. J. Am. Chem. Soc. 113, 5131–5133 (1991).
7. Sherman, W. B. & Seeman, N. C. A precisely controlled DNA biped walking device. Nano Lett. 4, 1203–1207 (2004).
8. Sauvage, J.-P. (ed.) Molecular Machines and Motors (Structure and Bonding, Vol. 99, Springer, Berlin, 2001).
9. van Delden, R. A., Koumura, N., Harada, N. & Feringa, B. L. Unidirectional rotary motion in a liquid crystalline environment: colour tuning by a molecular motor. Proc. Natl Acad. Sci. USA 99, 4945–4949 (2002).
10. Koumura, N., Geertsema, E. M., van Gelder, M. B., Meetsma, A. & Feringa, B. L. Second generation light-driven molecular motors. Unidirectional rotation controlled by a single stereogenic center with near-perfect photoequilibria and acceleration of the speed of rotation by structural modification. J. Am. Chem. Soc. 124, 5037–5051 (2002).
11. Liu, Y. et al. Linear artificial muscles. J. Am. Chem. Soc. 127, 9745–9759 (2005).
12. Zheng, X. et al. Dipolar and nonpolar altitudinal molecular rotors mounted on an Au(III) surface. J. Am. Chem. Soc. 126, 4540–4542 (2004).
13. Kottas, G. S., Clarke, L. I. & Horinek, D. Michl, J. Artificial molecular rotors. Chem. Rev. 105, 1281–1376 (2005).
14. Koumura, N., Geertsema, E. M., Meetsma, A. & Feringa, B. L. Light-driven molecular rotor: unidirectional rotation controlled by a single stereogenic center. J. Am. Chem. Soc. 122, 12005–12006 (2000).
15. Noji, H., Yasuda, R., Yoshida, M. & Kinosita, K. Direct observation of the rotation of F₁-ATPase. Nature 386, 299–302 (1997).
16. George Thomas, K. & Kamat, P. V. Chromophore-functionalised gold nanoparticles. Acc. Chem. Res. 36, 888–898 (2003).
17. Manna, A. et al. Optimised photoisomerisation on gold nanoparticles capped by unsymmetrical azobenzene disulfides. Chem. Mater. 15, 20–28 (2003).
18. Long, B., Nikitin, K. & Fitzmaurice, D. Assembly of an electronically switchable rotaxane on the surface of a titanium dioxide nanoparticle. J. Am. Chem. Soc. 125, 15490–15498 (2003).
19. Brust, M., Walker, M., Bethell, D., Schiffrin, D. J. & Whyman, R. J. Synthesis of thiol-derivatised gold nanoparticles in a 2-phase liquid-liquid system. Chem. Soc. Chem. Comm., 801–802 (1994).
20. Lide, D. R. (ed.) CRC Handbook of Chemistry and Physics 2003–2004 84th edn 4–59 (CRC Press, Boca Raton, 2003).
21. Ulman, A. Formation and structure of self-assembled monolayers. Chem. Rev. 96, 1533–1554 (1996).

Low-latitude seasonality of Cretaceous temperatures in warm and cold episodes

Thomas Steuber[1], Markus Rauch[1], Jean-Pierre Masse[2], Joris Graaf[3] & Matthias Malkoč[1]

The Cretaceous period is generally considered to have been a time of warm climate[1–6]. Evidence for cooler episodes exists, particularly in the early Cretaceous period[6–8], but the timing and significance of these cool episodes are not well constrained. The seasonality of temperatures is important for constraining equator-to-pole temperature gradients and may indicate the presence of polar ice sheets; however, reconstructions of Cretaceous sea surface temperatures are predominantly based on the oxygen isotopic composition of planktonic foraminifera[1–4] that do not provide information about such intra-annual variations. Here we present intra-shell variations in δ¹⁸O values of rudist bivalves (Hippuritoidea) from palaeolatitudes between 8° and 31° N, which record the evolution of the seasonality of Cretaceous sea surface temperatures in detail. We find high maximum temperatures (~35 to 37 °C) and relatively low seasonal variability (<12 °C) between 20° and 30° N during the warmer Cretaceous episodes. In contrast, during the cooler episodes our data show seasonal sea surface temperature variability of up to 18 °C near 25° N, comparable to the range found today. Such a large seasonal variability is compatible with the existence of polar ice sheets.

The Cretaceous was a period of warm climate, with mid-Cretaceous (100–88 million years, Myr, ago) polar sea surface temperature (SST) as high as 20 °C (ref. 9). Although there is evidence for polar ice in the early Cretaceous[6–8], greenhouse conditions of Earth's climate system during the middle and late Cretaceous are supported by a plethora of geological, palaeontological and geochemical data[9]. Geochemical proxies, including δ¹⁸O values of foraminifera, fish teeth and the composition of membrane lipids[1–4,9–11], are from biological materials that do not provide data on sub-annual timescales. Reconstructed Cretaceous SSTs are thus believed to represent annual averages, although the seasonal timing of formation of the studied biological materials is not known. Estimates of terrestrial seasonality based on fossil floras are an exception, but are only available for a few localities[12].

We have analysed intra-shell variations in isotopic (δ¹⁸O, δ¹³C) and chemical (Mg, Sr, Fe, Mn) compositions of shells of rudist bivalves from localities (Fig. 1) in the Caribbean, the peri-Mediterranean region and the Middle East (8–31° N palaeolatitude, 85° W–31° E palaeolongitude). Numerical ages for most studied localities were obtained by strontium isotope stratigraphy[13], the others have a precise biostratigraphical control. Details of localities, stratigraphy and taxonomy of the studied shells are available as Supplementary Information. Most of our data are from 15–30° N palaeolatitude (Fig. 1), and thus from regions that must have experienced the highest seasonal temperature extremes. Rudist bivalves inhabited marine subtidal environments well above the thermocline[14]. In contrast to foraminifera, which have been the main source of proxy data on Cretaceous SST, the outer shell layer of certain groups of rudist is compact (see Supplementary Information), and has a

large potential to preserve the original chemical and isotopic composition[15,16]. Modern bivalve molluscs reliably record temperature-dependent fractionation of oxygen isotopes in the δ¹⁸O values of their shell carbonates[17,18]. Metabolic effects can thus be largely ruled out for rudist bivalves, although pronounced disequilibrium fractionation has been reported for a single genus[15].
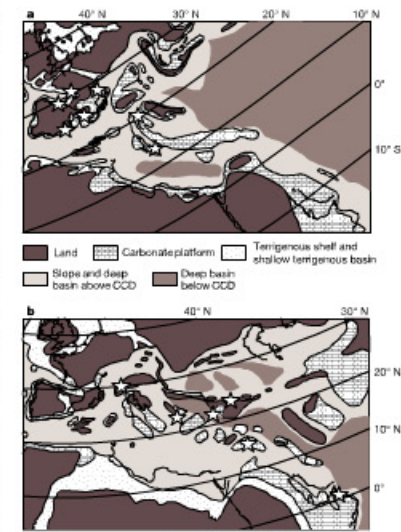

Figure 1 | Palaeo-positions of localities studied. White stars indicate localities; those in the Caribbean (Jamaica) are not shown. Modern coastlines—that is, of Great Britain in the upper left, and the Arabian Gulf in the lower right, of the maps—are given for orientation. **a**, Localities from 120–91 Myr ago plotted on early Aptian (119 Myr ago) palaeogeography, modified from ref. 25. **b**, Localities from 90–66 Myr ago plotted on Maastrichtian (67 Myr ago) palaeogeography, modified from ref. 26. See Supplementary Information for precise palaeolatitudes.

¹Institut für Geologie, Mineralogie und Geophysik, Ruhr-Universität, 44801 Bochum, Germany. ²Centre de Sédimentologie-Paléontologie, Université de Provence, 13331 Marseille Cedex 03, France. ³Department of Earth and Life Sciences, Vrije Universiteit, De Boelelaan 1085, 1081 HV Amsterdam, The Netherlands.